

EntroAD: Structural Entropy-Guided Prompt Adaptation for Zero-Shot Anomaly Detection

Xinyu Zhao
Beihang University
Beijing, China
xyzhao@buaa.edu.cn

Qingyun Sun*
Beihang University
Beijing, China
sunqy@buaa.edu.cn

Jiayi Luo
Beihang University
Beijing, China
luojy@buaa.edu.cn

Jianxin Li
Beihang University
Beijing, China
lijx@buaa.edu.cn

Abstract

Zero-Shot Anomaly Detection (ZSAD) aims to detect anomalies in unseen domains without target-domain adaptation. Recent CLIP-based methods have shown promising performance by leveraging prompt learning and visual-text alignment. However, most existing approaches rely on a single adaptation pathway, which may be insufficient for heterogeneous anomaly patterns across domains. In practice, anomalies exhibit vastly different characteristics, ranging from salient, localized structural disruptions to subtle, diffuse, and irregular variations. To address this challenge, we propose **EntroAD**, a structural entropy-guided zero-shot anomaly detection framework. Unlike previous methods, EntroAD introduces a dynamic routing mechanism to process different types of anomalies with specialized adaptation strategies. Specifically, we estimate patch-level structural entropy from self-attention-induced patch relations and use it as a proxy for relational uncertainty to guide anomaly-aware token routing. Based on this routing signal, we construct anomaly-aware routed tokens to better capture anomaly cues with different structural characteristics. We further introduce a confidence-aware dual-branch prompt adaptation module to stabilize visual-text alignment while preserving CLIP’s transferable prior. Extensive experiments on 10 industrial and medical benchmarks show that EntroAD achieves state-of-the-art performance in challenging cross-dataset ZSAD settings.

CCS Concepts

• **Computing methodologies** → **Scene anomaly detection.**

Keywords

CLIP, Anomaly Detection, Structural Entropy, Zero-shot

1 Introduction

Anomaly detection (AD) aims to model normal visual patterns and identify irregular instances, such as defects in industrial manufacturing [2, 38] or abnormalities in medical imaging [9]. Recent advances in visual representation learning have enabled AD methods [5, 6, 14, 20, 24, 33] to achieve strong performance with sufficient in-domain data. However, these methods are typically tied to domain-specific data distributions, which limits their practicality in real-world deployment. In practice, collecting large-scale annotations for every product category, imaging device, or clinical modality is costly and often infeasible. This challenge has made Zero-Shot Anomaly Detection (ZSAD) increasingly important, as it seeks to transfer anomaly knowledge to unseen target domains

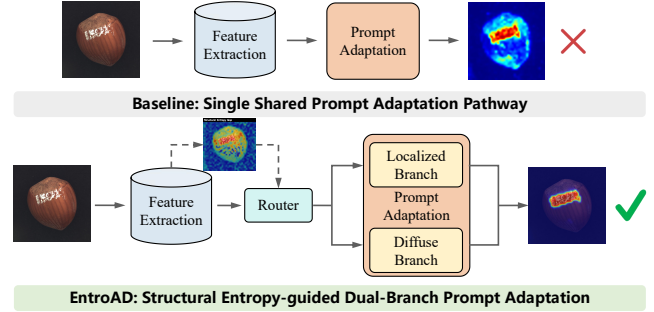


Figure 1: Conceptual comparison between the baseline and EntroAD. Top: Existing methods rely on a single shared prompt adaptation pathway, which often leads to noisy localization. Bottom: EntroAD introduces a structural entropy router. By explicitly quantifying relational uncertainty via structural entropy maps (as shown for the hazelnut defect), our framework dynamically directs anomaly-aware tokens into a specialized dual-branch adaptation module for precise visual-text alignment.

without target-domain adaptation. Despite recent progress, existing ZSAD methods still struggle to generalize across domains with substantially different structural and semantic anomaly patterns, such as localized surface scratches, missing components, or diffuse pathological variations.

Recently, Contrastive Language-Image Pretraining (CLIP) [23] has shown strong transfer ability in open-vocabulary recognition and zero-shot perception [32, 34], making it a natural foundation for ZSAD. Accordingly, recent ZSAD methods adapt CLIP representations to distinguish normal and anomalous patterns. One line of work enhances textual guidance with prompts specifically related to anomalies. For instance, WinCLIP [15] uses manually designed prompts, while later methods such as AnomalyCLIP [35], FiLo [11], and FAPrompt [36] further refine the text space with learnable or fine-grained prompts. Another line introduces visual adapters to reduce the cross-modal gap for anomalous features, including April-GAN [4], AA-CLIP [21], and AdaptCLIP [10]. Despite their effectiveness, most methods rely on a shared alignment strategy and rarely consider relational uncertainty among patches.

Such a shared adaptation paradigm (Figure 1) becomes brittle because it overlooks a critical bottleneck in cross-domain ZSAD: the unquantified relational uncertainty among image patches. While existing cues capture semantic abnormality or patch-text similarity, they fail to model how different anomalies—ranging from sharp structural defects to diffuse pathological variations—disrupt local

*Corresponding author.

patch interactions differently under domain shift. For instance, a localized scratch disrupts regular interactions abruptly, whereas diffuse irregularities scatter them broadly. This missing relation-aware uncertainty makes a fixed adaptation pathway insufficient for cross-domain generalization, inevitably leading to weaker visual-text correspondence and noisy anomaly localization.

To address this limitation, we argue that ZSAD should not rely on a single, uniform adaptation pathway. The primary bottleneck is that a shared strategy ignores the relational uncertainty of local patch interactions, making it unable to generalize across heterogeneous anomaly patterns. Motivated by this insight, we propose **EntroAD**, a structural entropy-guided zero-shot anomaly detection framework (Figure 1). Specifically, we introduce a structural entropy router that estimates patch-level structural entropy from self-attention to explicitly characterize this relational uncertainty. We observe that high entropy reflects dispersed and uncertain interactions, while low entropy indicates stable local structure; thus, entropy serves as a compact and interpretable descriptor of relational instability. Although different anomalies vary visually, they both give rise to characteristic variations in structural entropy that act as a powerful routing prior. Based on these behaviors, EntroAD uses structural entropy to construct anomaly-aware tokens via soft routing and confidence-aware aggregation. This allows patches with different uncertainty patterns to contribute specializedly to downstream alignment, rather than being forced through a uniform pathway. Furthermore, since heterogeneous uncertainty can bias a single adaptation branch, we introduce a dual-branch prompt adaptation module. This parallel design provides complementary alignment signals for both localized and diffuse anomalies while preserving CLIP’s transferable prior. Extensive experiments on 10 benchmarks demonstrate that by explicitly modeling relational uncertainty, EntroAD achieves state-of-the-art performance in cross-domain anomaly localization.

Our main contributions are summarized as follows:

- We propose EntroAD, a novel framework for zero-shot anomaly detection. To overcome the limitation of uniform adaptation strategies, we introduce a structural entropy-guided token routing mechanism that leverages patch-level relational uncertainty to selectively aggregate anomaly-relevant tokens, enabling better handling of diverse anomaly patterns.
- We develop a confidence-aware dual-branch prompt adaptation module for anomaly localization. By providing separate visual-text alignment pathways for structural defects and diffuse anomalies, the module mitigates adaptation bias while preserving the transferable prior of CLIP.
- Extensive experiments on 10 industrial and medical benchmarks demonstrate that EntroAD achieves state-of-the-art performance under challenging cross-dataset zero-shot settings.

2 Related Work

2.1 Zero-Shot Anomaly Detection

Zero-shot anomaly detection (ZSAD) aims to detect anomalies in unseen categories without target-specific fine-tuning. With its strong open-vocabulary transfer ability, CLIP [23] has become a major

foundation for recent ZSAD methods. WinCLIP [15] is an early representative work that measures the similarity between handcrafted anomaly prompts and multi-scale image patches. Since then, most CLIP-based ZSAD methods have mainly improved anomaly detection in four directions: prompt learning, visual adaptation, joint cross-modal adaptation, and retrieval-based modeling.

For prompt learning, AnomalyCLIP [35] and FiLo [11] replace handcrafted prompts with learnable prompt parameters, while AdaCLIP [3] adopts a hybrid prompt design to improve text-patch alignment. To describe anomalies with richer semantics, FAPrompt [36] further introduces fine-grained and decomposed abnormality prompts instead of relying only on coarse anomaly descriptions. For visual adaptation, April-GAN [4] introduces linear adapters to project pretrained visual features, and AA-CLIP [21] combines residual adaptation with a separability-enhancing objective to refine patch representations. Beyond adapting only one side, AF-CLIP [8] and AdaptCLIP [10] jointly optimize visual and textual spaces to improve anomaly-aware alignment. Different from these parametric adaptation methods, MRAD [31] proposes a memory-driven retrieval framework that freezes the CLIP encoder and infers anomaly scores through hierarchical memory matching on auxiliary data.

Despite their effectiveness, most CLIP-based ZSAD methods rely on a shared alignment strategy, without explicitly modeling relational uncertainty among patches. Such a uniform paradigm often struggles to capture structurally heterogeneous anomalies across domains.

2.2 Structural Entropy

Structural entropy was originally introduced to describe the complexity and organization of graph-structured data [19, 27]. While classical information entropy typically measures the uncertainty of independent elements, the concept of structural entropy emphasizes the stability and organization of relations among connected nodes [19, 30]. Because of this property, entropy-based graph analysis has been widely used to reveal local irregularities and hidden structural patterns in complex networks [29, 37].

Although structural uncertainty has been explored in graph-based tasks, its potential in vision-language modeling remains largely untapped. In Vision Transformers (ViTs) [7], self-attention naturally captures dense interactions among image patches, forming an implicit patch-level relation graph. Inspired by the concept of structural entropy, we propose to quantify the relational uncertainty of this visual graph by calculating the information entropy of local attention distributions. To the best of our knowledge, utilizing such structural entropy as a routing signal for patch-level anomaly alignment remains unexplored. In our setting, this perspective is particularly relevant because anomaly localization depends not only on whether a patch appears abnormal, but also on whether its local structural relations become unstable or uncertain under cross-domain shifts.

3 Notations and Problem Formulation

Let $\mathcal{X} \subset \mathbb{R}^{H \times W \times C}$ denote the image space. In zero-shot anomaly detection (ZSAD), a model F_Θ is trained on a source-domain dataset $\mathcal{D}_{\text{train}} = \{(x_i, y_i, Y_i)\}_{i=1}^{N_{\text{train}}}$, where $x_i \in \mathcal{X}$ is an image, $y_i \in \{0, 1\}$ is its image-level label, and $Y_i \in \{0, 1\}^{H \times W}$ is the pixel-level mask. The

objective is to learn transferable representations that can be directly evaluated on a collection of unseen target datasets $\{\mathcal{D}_{\text{test}}^1, \dots, \mathcal{D}_{\text{test}}^n\}$ containing disjoint semantic categories, without any target-domain adaptation. Given a test image $x \in \mathcal{D}_{\text{test}}^j$, the model predicts an image-level anomaly score $a \in \mathbb{R}$ and a pixel-level localization map $\mathbf{M} \in \mathbb{R}^{H \times W}$, denoted as $(a, \mathbf{M}) = F_{\Theta}(x)$.

4 Methodology

To address the limitations of shared alignment strategies in handling structurally heterogeneous anomaly patterns across diverse domains, we propose EntroAD, a structural entropy-guided prompt adaptation framework for zero-shot anomaly detection. As illustrated in Figure 2, rather than forcing all visual features into a uniform adaptation pathway, our approach explicitly leverages relational uncertainty to adaptively route patch features, followed by a dual-branch module to capture diverse anomaly cues.

Specifically, given an input image, the frozen visual encoder extracts dense patch features and multi-layer self-attention maps. The EntroAD framework then refines cross-domain anomaly localization through a two-stage process. In Stage 1, a source-domain memory bank concurrently provides base retrieval-guided image-level and patch-level anomaly evidence. Building upon these foundational representations, Stage 2 further refines the alignment through three consecutive steps: (1) estimating patch-level structural entropy to explicitly quantify relational uncertainty; (2) performing entropy-guided routing and confidence-aware gating to aggregate raw patches into a compact pair of normal and anomaly tokens; and (3) adapting textual prompts via the dual-branch module to achieve precise, anomaly-aware visual-text alignment. Finally, during inference, the branch-specific anomaly maps and the base retrieval scores are synergistically fused to output the ultimate pixel-level localization map and image-level anomaly score.

4.1 Structural Entropy from Visual Attention

Our framework uses a Vision Transformer (ViT) visual encoder within CLIP. Besides the token features themselves, we exploit self-attention to characterize patch-level relational uncertainty. For transformer layer ℓ , let $\mathbf{A}^{(\ell)} \in \mathbb{R}^{(N+1) \times (N+1)}$ denote the head-averaged self-attention matrix, where the extra token corresponds to the global [CLS] token. We remove the [CLS] token and row-normalize the remaining spatial attention map to obtain $\tilde{\mathbf{A}}^{(\ell)} \in \mathbb{R}^{N \times N}$, whose rows define patch-wise attention distributions [28]:

$$\tilde{A}_{ij}^{(\ell)} = \frac{A_{ij}^{(\ell)}}{\sum_{j'=1}^N A_{ij'}^{(\ell)} + \epsilon}, \quad (1)$$

where ϵ is a small constant for numerical stability.

The structural entropy of the i -th patch at layer ℓ is computed using the standard information entropy formulation [19, 26]:

$$e_i^{(\ell)} = - \sum_{j=1}^N \tilde{A}_{ij}^{(\ell)} \log(\tilde{A}_{ij}^{(\ell)} + \epsilon), \quad (2)$$

which serves as a proxy for the uncertainty of attention-induced patch relations. We then average the entropy values over selected

visual layers Ω to obtain the final patch-level structural entropy:

$$e_i = \frac{1}{|\Omega|} \sum_{\ell \in \Omega} e_i^{(\ell)}, \quad \mathbf{e} = [e_1, e_2, \dots, e_N]^T. \quad (3)$$

Intuitively, low entropy indicates that a patch mainly interacts with a compact and stable set of neighbors, which is typical for regular normal backgrounds. In contrast, both localized structural defects and diffuse irregularities disrupt these regular patch interactions, inducing relational instability and yielding higher structural entropy relative to their surrounding normal regions.

The key distinction lies in their spatial distribution: a sharp defect typically manifests as a concentrated high-entropy spike, whereas a diffuse abnormality forms a broad, irregular high-entropy region. Therefore, we use \mathbf{e} as an interpretable routing prior to identify structurally unstable regions as anomaly candidates, while the subsequent dual-branch module is responsible for modeling their distinct spatial characteristics.

4.2 Entropy-Guided Token Routing and Confidence-Aware Gating

This stage aggregates informative normal and anomaly tokens from dense patch features. Let $\{z_i\}_{i=1}^N$ denote the dense patch features extracted by the visual encoder for downstream alignment, and $\{r_i\}_{i=1}^N$ denote the projected patch features from the Stage 1 base memory-guided retrieval branch. Instead of uniform pooling, we combine patch-level retrieval evidence from a source-domain patch-level memory bank with structural entropy to obtain adaptive routing weights. Specifically, the memory bank is parameterized by keys \mathbf{K}_{pat} representing memory prototypes, and values \mathbf{V}_{pat} storing their associated normal/anomaly label vectors.

Patch-Wise Anomaly Evidence. For each projected patch feature r_i , we compute its similarity to the patch-level memory keys as

$$\mathbf{s}_i = r_i \mathbf{K}_{pat}^T, \quad (4)$$

where $\mathbf{K}_{pat} \in \mathbb{R}^{M \times d}$ denotes M memory prototypes. To mitigate the dominance of overly common background patterns, we apply quantile-based filtering to the similarities before softmax normalization. The normalized retrieval weights are then multiplied by the memory values to compute a normal/anomaly response vector $\mathbf{o}_i = \text{softmax}(\mathbf{s}_i) \mathbf{V}_{pat} = [o_{i,n}, o_{i,a}]$. The patch-wise anomaly pseudo-probability is defined as $p_i = o_{i,a}$.

Entropy-Guided Soft Routing. We first normalize the structural entropy values within each image to $\hat{e}_i \in [0, 1]$ using standard min-max scaling: $\hat{e}_i = (e_i - \min_j e_j) / (\max_j e_j - \min_j e_j + \epsilon)$. To form compact representations, we define the routing logits r_i^a and r_i^n for anomalous and normal token aggregation as:

$$r_i^a = \frac{p_i \hat{e}_i}{T}, \quad r_i^n = \frac{(1 - p_i)(1 - \hat{e}_i)}{T}, \quad (5)$$

where T is a temperature parameter. By applying a spatial softmax over the N patches, we convert these logits into normalized routing weights w_i^a and w_i^n .

Finally, using the high-level patch features $\{z_i\}_{i=1}^N$, we aggregate them into a singular normal token \mathbf{t}_n and a raw anomaly token \mathbf{t}_a^{raw}

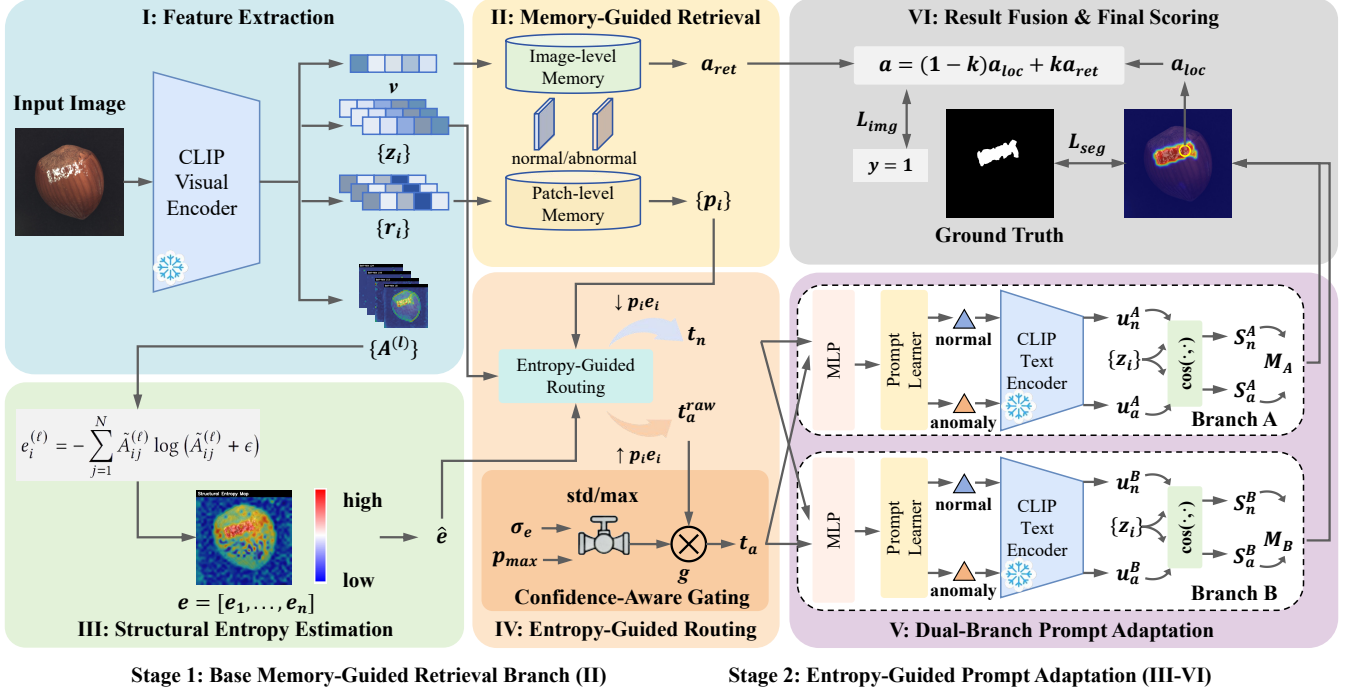


Figure 2: The overall architecture of the EntroAD framework. (I) Feature Extraction: Multi-scale patch features and self-attention maps are extracted from a frozen CLIP visual encoder. Then, the framework operates in two main stages for anomaly detection. **Stage 1: Base Memory-Guided Retrieval (II):** A source-domain memory bank computes patch-wise anomaly evidence and image-level retrieval scores. **Stage 2: Entropy-Guided Prompt Adaptation (III-VI):** (III) **Structural Entropy Estimation** (Sec. 4.1): Patch-level structural entropy is derived from visual self-attention to explicitly quantify relational uncertainty as a routing prior. (IV) **Entropy-Guided Routing** (Sec. 4.2): Dense features are adaptively aggregated into compact tokens with a confidence-aware gating mechanism. (V) **Dual-Branch Prompt Adaptation** (Sec. 4.3): Routed tokens generate branch-specific prompt biases to dynamically refine visual-text alignment. (VI) **Result Fusion & Final Scoring** (Sec. 4.4): During inference, the image-level retrieval scores and pixel-level localization maps are synergistically fused for the final prediction.

via weighted summation:

$$\mathbf{t}_n = \sum_{i=1}^N w_i^n z_i, \quad \mathbf{t}_a^{raw} = \sum_{i=1}^N w_i^a z_i. \quad (6)$$

This routing mechanism elegantly encourages the anomaly token to focus on patches that are both retrieval-salient and structurally uncertain, while the normal token emphasizes stable and low-entropy regions.

Confidence-Aware Gating. To improve robustness under domain shift, we further suppress unreliable anomaly evidence with a confidence-aware gate. Let $p_{max} = \max_i p_i$ be the maximum anomaly confidence and let $\sigma_e = \text{Std}(\hat{e})$ denote the standard deviation of normalized entropy. We define

$$g = \text{sigmoid}((p_{max} - \tau)(k_0 + k_1\sigma_e)), \quad (7)$$

where τ , k_0 , and k_1 are scalar parameters. The final anomaly token is then given by

$$\mathbf{t}_a = g \cdot \mathbf{t}_a^{raw}. \quad (8)$$

The resulting token pair $\{\mathbf{t}_n, \mathbf{t}_a\}$ serves as the input to the downstream prompt adaptation module.

4.3 Dual-Branch Prompt Adaptation

After routing, we obtain a compact pair of normal and anomaly tokens that summarizes the current image. We then feed them into a dual-branch prompt adaptation module. The two branches share the same architecture but use independent parameters, allowing them to provide complementary prompt adaptation signals while maintaining a simple and transferable design. Each branch takes the routed token pair as input and produces a branch-specific prompt bias that is injected into the prompt learner, thereby refining text representations in an image-adaptive manner while preserving CLIP’s transferable prior.

Dual-Branch Prompt Bias Generation. Given the routed token pair $\{\mathbf{t}_n, \mathbf{t}_a\}$, the two branches generate branch-specific prompt biases

$$\mathbf{b}^A = f_A(\mathbf{t}_n, \mathbf{t}_a), \quad \mathbf{b}^B = f_B(\mathbf{t}_n, \mathbf{t}_a), \quad (9)$$

where $f_A(\cdot)$ and $f_B(\cdot)$ have identical architecture but independent parameters. In practice, each branch is implemented as a lightweight two-layer MLP operating on the routed token pair. This design allows the two branches to capture complementary adaptation

Algorithm 1: Training Procedure of EntroAD

Input: Source-domain training set $\mathcal{D} = \{(x, y, Y)\}$
Output: Trained EntroAD

// Stage 1: Base Memory-Guided Retrieval Branch

Freeze the CLIP visual backbone;

Optimize the visual projection modules with the Stage-1 objective in Eq. (17);

// Stage 2: Entropy-Guided Prompt Adaptation

Freeze the visual backbone and the Stage-1 visual projection modules;

for each minibatch $(x, y, Y) \in \mathcal{D}$ **do**

 Extract patch features $\{z_i\}_{i=1}^N$, projected patch features

 $\{r_i\}_{i=1}^N$, and attention maps $\{A^{(\ell)}\}_{\ell \in \Omega}$;

 Compute patch-wise anomaly evidence $\{p_i\}$ using the base memory-guided retrieval branch;

 Estimate structural entropy \mathbf{e} by Eq. (2) and Eq. (3);

 Perform entropy-guided routing and confidence-aware gating to obtain (t_n, t_a) by Eq. (5)–Eq. (8);

 Generate branch-specific prompt biases \mathbf{b}^A and \mathbf{b}^B by Eq. (9);

Synthesize branch-specific prompts, compute text embeddings, and obtain branch-specific anomaly maps by Eq. (10)–Eq. (12);

Compute the branch losses and the Stage-2 objective in Eq. (18) and Eq. (19);

Update the prompt learner and the dual-branch prompt adaptation module;

return Trained model;

tendencies under heterogeneous anomaly patterns, rather than forcing all samples into a single prompt adaptation mode.

Prompt Synthesis and Text Encoding. Given a branch-specific bias \mathbf{b}^m for branch $m \in \{A, B\}$, we add \mathbf{b}^m to the learnable context tokens of the prompt learner to generate a normal prompt and an anomaly prompt for branch m . The CLIP text encoder then encodes the resulting prompts:

$$\mathbf{u}_n^m = \text{Enc}_t(\mathbf{p}_n(\mathbf{b}^m)), \quad \mathbf{u}_a^m = \text{Enc}_t(\mathbf{p}_a(\mathbf{b}^m)), \quad (10)$$

where \mathbf{u}_n^m and \mathbf{u}_a^m denote the normalized text embeddings for the normal and anomaly prompts, respectively.

Branch-Specific Anomaly Maps. To achieve robust and discriminative localization, we compute branch-specific anomaly maps from the adapted text embeddings. Let $\mathbf{Z}^{(\ell)} \in \mathbb{R}^{N \times d}$ denote the dense patch features from a selected visual layer $\ell \in \Omega_{map}$. For each branch m , we compute the cosine similarity between the patch features and the branch-specific text embeddings, followed by a softmax normalization along the class dimension. This yields the layer-wise normal probability map $S_n^{m,\ell}$ and anomaly probability map $S_a^{m,\ell}$:

$$[S_n^{m,\ell}, S_a^{m,\ell}] = \text{softmax} \left(\frac{\mathbf{Z}^{(\ell)}(\mathbf{u}_n^m)^\top}{\tau_s}, \frac{\mathbf{Z}^{(\ell)}(\mathbf{u}_a^m)^\top}{\tau_s} \right), \quad (11)$$

where τ_s is a temperature scaling factor. To enhance robustness, we aggregate the anomaly probability maps across multiple layers

to capture complementary semantic granularity. The final branch-specific anomaly map \mathbf{M}_m is obtained as:

$$\mathbf{M}_m = \frac{1}{|\Omega_{map}|} \sum_{\ell} S_a^{m,\ell}. \quad (12)$$

The resulting map $\mathbf{M}_m \in [0, 1]^N$ is naturally bounded as valid probabilities. It is then reshaped to the spatial grid and resized to the input resolution for subsequent fusion and supervision. Crucially, instead of discarding the normal probability maps $S_n^{m,\ell}$, we preserve them for explicit normal-suppression supervision during training (detailed in Sec. 4.4).

4.4 Training and Inference

Training Supervision. For each source-domain training sample, we denote the input as (x, y, Y) , where $y \in \{0, 1\}$ is the image-level anomaly label and $Y \in \{0, 1\}^{H \times W}$ is the pixel-level anomaly mask. Let $\hat{a}_{img} \in [0, 1]$ denote the predicted image-level anomaly probability, and let $\hat{\mathbf{M}} \in [0, 1]^{H \times W}$ denote a predicted anomaly map after resizing to the ground-truth resolution when needed.

Loss Functions. For image-level supervision, we use binary cross-entropy:

$$\mathcal{L}_{img} = -y \log(\hat{a}_{img} + \epsilon) - (1 - y) \log(1 - \hat{a}_{img} + \epsilon). \quad (13)$$

For pixel-level anomaly localization, we use the combination of focal loss and Dice loss. Given a predicted anomaly map $\hat{\mathbf{M}}$ and a binary mask Y , the focal loss is

$$\begin{aligned} \mathcal{L}_{focal}(\hat{\mathbf{M}}, Y) = & -\frac{1}{HW} \sum_{u=1}^H \sum_{v=1}^W \left[\alpha_f Y_{uv} (1 - \hat{M}_{uv})^\gamma \log(\hat{M}_{uv} + \epsilon) \right. \\ & \left. + (1 - \alpha_f)(1 - Y_{uv}) \hat{M}_{uv}^\gamma \log(1 - \hat{M}_{uv} + \epsilon) \right], \end{aligned} \quad (14)$$

where α_f is the class-balancing factor and γ is the focusing parameter.

The Dice loss is defined as

$$\mathcal{L}_{dice}(\hat{\mathbf{M}}, Y) = 1 - \frac{2 \sum_{u,v} \hat{M}_{uv} Y_{uv} + \epsilon}{\sum_{u,v} \hat{M}_{uv} + \sum_{u,v} Y_{uv} + \epsilon}. \quad (15)$$

The segmentation loss for any anomaly map is then written as

$$\mathcal{L}_{seg}(\hat{\mathbf{M}}, Y) = \mathcal{L}_{focal}(\hat{\mathbf{M}}, Y) + \lambda_d \mathcal{L}_{dice}(\hat{\mathbf{M}}, Y), \quad (16)$$

where λ_d controls the weight of the Dice term.

Stage-1 Objective. In the first stage, we optimize the base memory-guided retrieval branch, including the image-level retrieval pathway and the patch-level retrieval pathway. Let $\hat{\mathbf{M}}_{base}$ denote the anomaly map produced by the base segmentation branch. The Stage-1 objective is

$$\mathcal{L}_{stage1} = \mathcal{L}_{seg}(\hat{\mathbf{M}}_{base}, Y) + \mathcal{L}_{img}. \quad (17)$$

This stage establishes the source-domain retrieval evidence used later for entropy-guided token construction.

Stage-2 Objective. In the second stage, we freeze the visual backbone and the Stage-1 projection modules, and optimize the prompt learner together with the dual-branch prompt adaptation module. For each branch $m \in \{A, B\}$, we compute branch-specific similarity

Algorithm 2: Inference Procedure of EntroAD

Input: Target image x and trained EntroAD
Output: Image-level anomaly score a , pixel-level anomaly map \mathbf{M}

Extract patch features $\{\mathbf{z}_i\}_{i=1}^N$, projected patch features $\{\mathbf{r}_i\}_{i=1}^N$, and attention maps $\{\mathbf{A}^{(\ell)}\}_{\ell \in \Omega}$;
// Stage 1: Base Memory-Guided Retrieval Branch
Compute image-level retrieval score a_{ret} and patch-wise anomaly evidence $\{p_i\}$ using the base memory-guided retrieval branch;
// Stage 2: Entropy-Guided Prompt Adaptation
Estimate structural entropy \mathbf{e} by Eq. (2) and Eq. (3);
Perform entropy-guided routing and confidence-aware gating to obtain $(\mathbf{t}_n, \mathbf{t}_a)$ by Eq. (5)–Eq. (8);
Generate branch-specific prompt biases, synthesize branch-specific prompts, and obtain anomaly maps \mathbf{M}_A and \mathbf{M}_B by Eq. (9)–Eq. (12);
Fuse the branch-specific maps to obtain the final anomaly map \mathbf{M} by Eq. (20);
Compute the final image-level anomaly score a by Eq. (22);
return a, \mathbf{M} ;

maps over selected visual layers and supervise them with a branch loss:

$$\mathcal{L}_{clip}^m = \sum_{\ell \in \Omega_{map}} \left[\mathcal{L}_{focal}(\hat{\mathbf{M}}_a^{m,\ell}, \mathbf{Y}) + \lambda_d \mathcal{L}_{dice}(\hat{\mathbf{M}}_a^{m,\ell}, \mathbf{Y}) + \lambda_d \mathcal{L}_{dice}(\hat{\mathbf{M}}_n^{m,\ell}, 1 - \mathbf{Y}) \right], \quad (18)$$

where $\hat{\mathbf{M}}_a^{m,\ell}$ and $\hat{\mathbf{M}}_n^{m,\ell}$ denote the anomaly and normal similarity maps of branch m at visual layer ℓ , and Ω_{map} denotes the set of visual layers used for prompt-supervised alignment. We apply focal and Dice supervision to the anomaly map, while supervising the normal map with Dice loss only, since the normal branch mainly serves as a complementary support signal for suppressing anomalous responses.

The overall Stage-2 objective is the weighted combination of the two branch losses:

$$\mathcal{L}_{stage2} = \bar{\lambda}_A \mathcal{L}_{clip}^A + \bar{\lambda}_B \mathcal{L}_{clip}^B, \quad (19)$$

where $\bar{\lambda}_A = \frac{\lambda_A}{\lambda_A + \lambda_B + \epsilon}$ and $\bar{\lambda}_B = \frac{\lambda_B}{\lambda_A + \lambda_B + \epsilon}$ are the normalized weights (with ϵ being a small constant for numerical stability).

Inference and Prediction Fusion. During inference, the two branches produce branch-specific anomaly maps \mathbf{M}_A and \mathbf{M}_B . We fuse them with normalized weights:

$$\mathbf{M} = \bar{\alpha} \mathbf{M}_A + \bar{\beta} \mathbf{M}_B, \quad (20)$$

where $\bar{\alpha} = \frac{\alpha}{\alpha + \beta + \epsilon}$ and $\bar{\beta} = \frac{\beta}{\alpha + \beta + \epsilon}$ are the normalized fusion weights (with ϵ being a small constant for numerical stability).

To obtain the image-level anomaly score, we first compute the mean of the top-1% values in the fused anomaly map:

$$a_{loc} = \frac{1}{|\mathcal{T}|} \sum_{(u,v) \in \mathcal{T}} M_{uv}, \quad (21)$$

where \mathcal{T} denotes the set of spatial locations corresponding to the top-1% largest values in \mathbf{M} . We then combine this localization score with the image-level retrieval score a_{ret} :

$$a = (1 - k)a_{loc} + ka_{ret}, \quad (22)$$

where $k \in [0, 1]$ balances localization evidence and image-level retrieval evidence.

5 Experiments

5.1 Experimental Settings

Datasets. We evaluate our method on 10 datasets spanning two major application domains: industrial anomaly detection and medical anomaly detection. For the industrial domain, we use 5 standard benchmarks: MVTec-AD [2], VisA [38], BTAD [22], DTD-Synthetic (DTD) [1], and MPDD [16]. These datasets cover a wide range of manufacturing defects across different textures and object categories. For the medical domain, we evaluate on five widely used datasets: BrainMRI [18], HeadCT [25], Br35H [12], Endo [13], and Kvasir [17]. Following the cross-dataset ZSAD setting [36], we train our model on MVTec-AD and directly evaluate it on the other nine datasets without any target-domain fine-tuning. For zero-shot evaluation on MVTec-AD, we instead use the model trained on VisA. This protocol provides a systematic evaluation of cross-dataset generalization across both industrial and medical anomaly detection tasks. We benchmark EntroAD against several representative CLIP-based ZSAD methods, including WinCLIP [15], AnomalyCLIP [35], FiLo [11], AA-CLIP [21], FAPrompt [36], and MRAD [31]. A comprehensive summary of dataset characteristics, including imaging modalities and sample distributions, is available in the Appendix.

Evaluation Metrics. Following common practice in anomaly detection, we evaluate performance at both the image and pixel levels. For image-level anomaly detection, we report the area under the receiver operating characteristic curve (AUROC) and average precision (AP). For pixel-level anomaly localization, we report pixel-level AUROC and the area under the per-region overlap curve (AUPRO). Together, these metrics assess the model’s ability to identify anomalous images and accurately localize defective regions.

Implementation Details. Following [35], we adopt the frozen CLIP ViT-L/14@336px backbone. Our two-stage training follows [31]: Stage 1 establishes robust normal representations via memory-guided visual projection, while Stage 2 freezes previous modules to optimize the prompt learner and dual-branch adaptation module. The dual-branch architecture explicitly handles heterogeneous defects: Branch A focuses on structured, localized anomalies, whereas Branch B identifies diffuse, global patterns. During inference, assuming the broad application domain (e.g., industrial manufacturing vs. medical imaging) is known as a task-level prior, we prioritize the corresponding branch for final predictions. Experiments are conducted on a single 32GB NVIDIA V100 GPU. Comprehensive details regarding multi-layer feature extraction, optimization hyperparameters (e.g., routing temperature, loss and inference weights), and post-processing are provided in the Appendix.

Table 1: Comparison with state-of-the-art zero-shot anomaly detection methods on image-level benchmarks. Results are reported as (AUROC, AP) (%). Best and second-best results are highlighted in bold and underlined, respectively.

Type	Dataset	WinCLIP [15] CVPR'23	AnomalyCLIP [35] ICLR'24	FiLo [11] ACM MM'24	AA-CLIP [21] CVPR'25	FAPrompt [36] ICCV'25	MRAD [31] ICLR'26	EntroAD Ours
Industrial	MVTec-AD	(90.4, 95.6)	(88.1, 95.1)	(87.4, 94.3)	(89.7, 94.8)	(91.0, 95.2)	<u>(93.0, 97.0)</u>	(93.3, 97.2)
	VisA	(75.5, 78.7)	(78.4, 82.2)	(79.6, 84.2)	(78.5, 82.0)	(82.5, 84.3)	<u>(83.2, 85.5)</u>	(84.7, 87.2)
	BTAD	(68.2, 70.9)	(81.8, 77.0)	(84.1, 92.0)	(93.3, 96.6)	(91.0, 89.7)	<u>(92.7, 90.5)</u>	<u>(92.7, 93.9)</u>
	DTD	(95.1, 97.7)	(93.5, 97.0)	(94.1, 98.0)	(94.3, 93.7)	(96.0, 98.3)	(95.0, 98.1)	<u>(95.8, 98.5)</u>
	MPDD	(61.5, 69.2)	(70.9, 79.1)	(72.2, 74.9)	(57.7, 67.0)	<u>(77.9, 81.7)</u>	<u>(78.4, 80.3)</u>	(79.7, 82.9)
Medical	BrainMRI	(86.5, 91.5)	(88.5, 91.3)	(86.0, 85.6)	(92.6, 94.9)	<u>(95.7, 95.7)</u>	(95.3, <u>96.2</u>)	(96.1, 96.9)
	HeadCT	(81.8, 80.2)	(87.8, 86.9)	(93.8, 93.4)	(88.4, 90.9)	(93.4, 92.9)	<u>(94.8, 95.4)</u>	(95.7, 96.4)
	Br35H	(81.0, 83.2)	(89.5, 90.0)	(93.6, 92.8)	(89.6, 91.1)	<u>(96.8, 96.6)</u>	(96.3, 96.5)	(97.0, 97.0)
Average	–	(80.0, 83.4)	(84.8, 87.3)	(86.4, 89.4)	(85.5, 88.9)	(90.5, 91.8)	<u>(91.1, 92.4)</u>	(91.9, 93.8)

Table 2: Comparison with state-of-the-art zero-shot anomaly detection methods on pixel-level benchmarks. Results are reported as (AUROC, AUPRO) (%). Best and second-best results are highlighted in bold and underlined, respectively.

Type	Dataset	WinCLIP [15] CVPR'23	AnomalyCLIP [35] ICLR'24	FiLo [11] ACM MM'24	AA-CLIP [21] CVPR'25	FAPrompt [36] ICCV'25	MRAD [31] ICLR'26	EntroAD Ours
Industrial	MVTec-AD	(82.3, 61.9)	(89.5, 83.0)	(90.2, 57.2)	(91.9, 84.6)	(90.7, 82.1)	<u>(92.6, 84.9)</u>	(92.8, 86.2)
	VisA	(73.2, 51.0)	(94.4, 86.7)	(95.7, 80.6)	(94.8, 81.4)	(95.7, 86.8)	<u>(94.9, 84.9)</u>	(94.8, 87.4)
	BTAD	(72.7, 27.3)	(90.8, 66.4)	(90.3, 52.8)	(93.9, 69.8)	<u>(95.9, 75.3)</u>	(96.9, 75.9)	<u>(96.1, 75.1)</u>
	DTD	(79.5, 51.5)	<u>(97.9, 92.3)</u>	(98.0, 77.5)	(97.0, 88.7)	<u>(98.2, 91.8)</u>	(98.1, 89.8)	(98.5, 92.6)
	MPDD	(71.2, 40.5)	(96.3, 90.0)	(93.9, 69.1)	(95.9, 86.4)	(95.6, 85.4)	<u>(97.4, 90.4)</u>	(97.9, 92.3)
Medical	Endo	(68.2, 28.3)	(83.4, 61.2)	(87.5, 66.2)	(88.0, 68.7)	(85.5, 65.3)	<u>(89.1, 73.7)</u>	(89.4, 73.9)
	Kvasir	(69.7, 24.5)	(79.3, 52.0)	<u>(85.0, 51.7)</u>	(82.7, 48.9)	(80.8, 46.7)	<u>(84.9, 52.7)</u>	(85.3, 53.5)
Average	–	(73.8, 40.7)	(90.2, 75.9)	(91.5, 65.0)	(92.0, 75.5)	(91.8, 76.2)	<u>(93.4, 78.9)</u>	(93.5, 80.1)

5.2 Comparison with State-of-the-Art Methods

For a fair comparison, all baselines are evaluated under a unified cross-dataset protocol using their official implementations, ensuring consistent source-domain training and target-domain evaluation settings.

The comprehensive results for image-level anomaly detection and pixel-level localization performance are summarized in Table 1 and Table 2, respectively. Overall, EntroAD consistently outperforms existing competitive methods across both industrial and medical benchmarks, demonstrating robust zero-shot generalization capabilities without relying on any target-specific fine-tuning.

Image-level Evaluation. As shown in Table 1, EntroAD establishes a new state of the art with an average 91.9% AUROC and 93.8% AP, surpassing the strongest baseline by 0.8% and 1.4%. It achieves top results on industrial datasets (MVTec-AD, VisA, MPDD) and exhibits pronounced advantages in the medical domain (BrainMRI, HeadCT, Br35H). Notably, EntroAD achieves significant gains in medical tasks, such as a 2.4% AUROC improvement on the BrainMRI dataset. This suggests that our structural entropy-guided routing is particularly adept at capturing subtle, non-salient pathological disruptions that traditional saliency-based methods often overlook. This confirms its reliability in identifying global anomalies under

substantial domain shifts. Exhaustive per-category results for all industrial benchmarks are further detailed in the Appendix.

Pixel-level Evaluation. For anomaly localization (Table 2), EntroAD yields the best overall performance with an average 93.5% AUROC and 80.1% AUPRO, improving AUPRO by 1.2% over MRAD. It achieves peak metrics on MVTec-AD, DTD, MPDD, and notably VisA, while consistently ranking first on medical benchmarks like Endo and Kvasir. These results demonstrate its capacity for highly accurate spatial localization across heterogeneous domains.

5.3 Ablation Study

We conduct ablation experiments to quantify the contributions of EntroAD’s key components: entropy-guided routing, confidence-aware gating, and dual-branch prompt adaptation. As shown in Table 3, the full model consistently achieves the best performance across all benchmarks, with notable gains in pixel-level localization.

Among all components, the confidence-aware gating mechanism plays the most critical role. Removing it leads to a substantial degradation on MVTec-AD pixel-level metrics, where AUROC/PRO drops from (92.8, 86.2) to (79.7, 42.8). This significant decline indicates that the gating mechanism is essential for suppressing unreliable anomaly activations and stabilizing localization under distribution shifts. Without such filtering, noisy responses propagate, degrading pixel-level precision. Entropy-guided routing also contributes

Table 3: Ablation study of the key components in EntroAD, including entropy-guided routing, confidence-aware gating, and dual-branch prompt adaptation. Results are reported as (AUROC, AP) (%) for image-level evaluation and (AUROC, AUPRO) (%) for pixel-level evaluation. The best performance in each column is highlighted in bold.

Variant	MVTec-AD		MPDD		BrainMRI	Br35H	Endo	Kvasir
	Image-level	Pixel-level	Image-level	Pixel-level	Image-level	Image-level	Pixel-level	Pixel-level
EntroAD	(93.3, 97.2)	(92.8, 86.2)	(79.7, 82.9)	(97.9, 92.3)	(96.1, 96.9)	(97.0, 97.0)	(89.4, 73.9)	(85.3, 53.5)
w/o Gating	(89.8, 95.3)	(79.7, 42.8)	(79.1, 81.8)	(97.5, 90.6)	(95.9, 96.5)	(97.3, 97.0)	(88.6, 72.9)	(84.4, 51.9)
w/o Entropy Routing	(93.0, 96.9)	(92.7, 84.1)	(81.0, 84.2)	(97.8, 91.5)	(95.9, 96.7)	(97.0, 96.7)	(89.0, 72.7)	(84.5, 52.3)
w/o Dual-branch	(93.1, 96.9)	(92.4, 84.5)	(80.3, 82.4)	(97.7, 90.8)	(95.7, 95.8)	(97.1, 96.6)	(87.7, 69.4)	(82.9, 48.6)

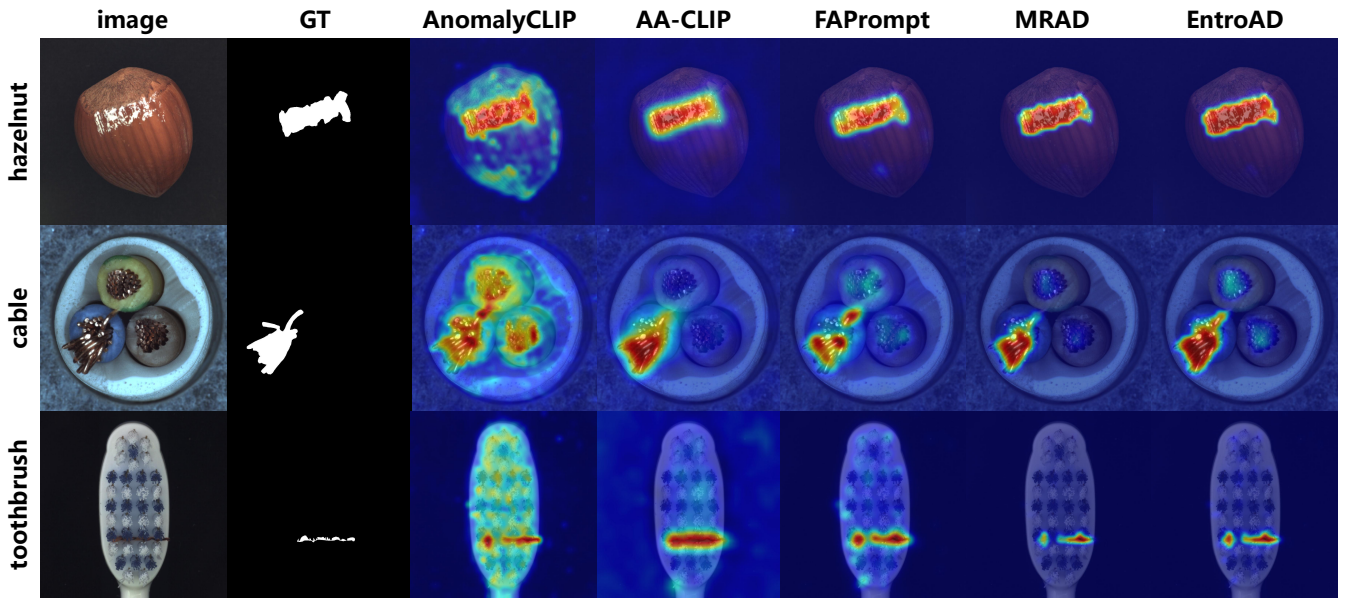


Figure 3: Qualitative comparison of anomaly localization results under the zero-shot setting. Compared with representative baselines, our EntroAD produces anomaly maps that are better aligned with the ground-truth (GT) masks.

to performance. Removing entropy guidance results in noticeable degradation on most pixel-level benchmarks. Although a marginal improvement is observed on MPDD image-level metrics, the overall performance becomes less stable. This suggests that structural entropy provides an effective inductive bias for prioritizing informative tokens, particularly in scenarios requiring fine-grained localization. Furthermore, replacing the dual-branch design with a single-branch variant leads to consistent performance drops, especially on medical datasets such as Endo and Kvasir. This observation highlights that the two branches capture complementary adaptation patterns: the primary branch focuses on structured anomalies, while the auxiliary branch enhances sensitivity to irregular and context-dependent patterns. Their combination improves cross-domain generalization and preserves robust visual-text alignment.

Overall, these results demonstrate that the proposed components are individually effective and highly complementary. Their integration is crucial for achieving strong and stable performance across diverse anomaly detection scenarios.

5.4 Visualization

Figure 3 presents qualitative comparisons of anomaly localization in the zero-shot setting. Compared to state-of-the-art baselines, EntroAD produces anomaly heatmaps that are more spatially concentrated and better aligned with ground-truth (GT) masks. Specifically, for the hazelnut sample, our method accurately focuses on the defective region with minimal response on the surrounding shell. In contrast, other baselines either over-activate irrelevant regions or fail to capture the full extent of the defect. Notably, our method precisely localizes anomalies while suppressing background noise, resulting in cleaner and more focused heatmaps, which is particularly beneficial for fine-grained anomaly localization.

6 Conclusion

In this paper, we propose EntroAD, a structural entropy-guided prompt adaptation framework for zero-shot anomaly detection. Built upon a CLIP-based memory-guided pipeline, our method integrates patch-level structural entropy estimation from visual self-attention, entropy-guided token routing with confidence-aware

gating, and dual-branch prompt adaptation for adaptive visual-text alignment. Extensive experiments on 10 industrial and medical benchmarks demonstrate that EntroAD achieves state-of-the-art zero-shot performance in both image-level detection and pixel-level localization. Overall, the results highlight the effectiveness of structural entropy-guided prompt adaptation for handling diverse anomaly patterns across domains.

References

- [1] Toshimichi Aota, Lloyd Teh Tzer Tong, and Takayuki Okatani. 2023. Zero-shot versus many-shot: Unsupervised texture anomaly detection. In *WACV*. 5564–5572.
- [2] Paul Bergmann, Michael Fauser, David Sattlegger, and Carsten Steger. 2019. MVTec AD—A comprehensive real-world dataset for unsupervised anomaly detection. In *CVPR*. 9592–9600.
- [3] Yunkang Cao, Jiangning Zhang, Luca Frittoli, Yuqi Cheng, Weiming Shen, and Giacomo Boracchi. 2024. Adaclip: Adapting clip with hybrid learnable prompts for zero-shot anomaly detection. In *ECCV*. Springer, 55–72.
- [4] Xuhai Chen, Yue Han, and Jiangning Zhang. 2023. April-gan: A zero-/few-shot anomaly classification and segmentation method for cvpr 2023 vand workshop challenge tracks 1&2: 1st place on zero-shot ad and 4th place on few-shot ad. *arXiv preprint arXiv:2305.17382* (2023).
- [5] Thomas Defard, Aleksandr Setkov, Angélique Loesch, and Romaric Audigier. 2021. Padim: a patch distribution modeling framework for anomaly detection and localization. In *ICPR*. Springer, 475–489.
- [6] Hanqiu Deng and Xingyu Li. 2022. Anomaly detection via reverse distillation from one-class embedding. In *CVPR*. 9737–9746.
- [7] Alexey Dosovitskiy, Lucas Beyer, Alexander Kolesnikov, Dirk Weissenborn, Xi-aohua Zhai, Thomas Unterthiner, Mostafa Dehghani, Matthias Minderer, Georg Heigold, Sylvain Gelly, et al. 2020. An image is worth 16x16 words: Transformers for image recognition at scale. *arXiv preprint arXiv:2010.11929* (2020).
- [8] Qingqing Fang, Wenxi Lv, and Qinliang Su. 2025. Af-clip: Zero-shot anomaly detection via anomaly-focused clip adaptation. In *ACM MM*. 4846–4855.
- [9] Tharindu Fernando, Harshala Gammulle, Simon Denman, Sridha Sridharan, and Clinton Fookes. 2021. Deep learning for medical anomaly detection—a survey. *CSUR* 54, 7 (2021), 1–37.
- [10] Bin-Bin Gao, Yue Zhou, Jiangtao Yao, Yuezhi Cai, Weixi Zhang, Meng Wang, Jun Liu, Yong Liu, Lei Wang, and Chengjie Wang. 2025. Adaptclip: Adapting clip for universal visual anomaly detection. *arXiv preprint arXiv:2505.09926* (2025).
- [11] Zhaopeng Gu, Bingke Zhu, Guibo Zhu, Yingying Chen, Hao Li, Ming Tang, and Jinqiao Wang. 2024. Filo: Zero-shot anomaly detection by fine-grained description and high-quality localization. In *ACM MM*. 2041–2049.
- [12] Ahmed Hamada. 2020. Br35h: Brain tumor detection 2020. *Kaggle Dataset* (2020).
- [13] Steven A Hicks, Debesh Jha, Vajira Thambawita, Pål Halvorsen, Hugo L Hammer, and Michael A Riegler. 2021. The EndoTect 2020 challenge: evaluation and comparison of classification, segmentation and inference time for endoscopy. In *ICLR*. Springer, 263–274.
- [14] Jeeho Hyun, Sangyun Kim, Giyoung Jeon, Seung Hwan Kim, Kyunghoon Bae, and Byung Jun Kang. 2024. Reconpatch: Contrastive patch representation learning for industrial anomaly detection. In *WACV*. 2052–2061.
- [15] Jongheon Jeong, Yang Zou, Taewan Kim, Dongqing Zhang, Avinash Ravichandran, and Onkar Dabeer. 2023. Winclip: Zero-/few-shot anomaly classification and segmentation. In *CVPR*. 19606–19616.
- [16] Stepan Jezek, Martin Jonak, Radim Burget, Pavel Dvorak, and Milos Skotak. 2021. Deep learning-based defect detection of metal parts: evaluating current methods in complex conditions. In *2021 13th International congress on ultra modern telecommunications and control systems and workshops (ICUMT)*. IEEE, 66–71.
- [17] Debesh Jha, Pia H Smedsrud, Michael A Riegler, Pål Halvorsen, Thomas De Lange, Dag Johansen, and Håvard D Johansen. 2019. Kvasir-seg: A segmented polyp dataset. In *MMM*. Springer, 451–462.
- [18] Pranita Balaji Kanade and PP Gumaste. 2015. Brain tumor detection using MRI images. *Brain* 3, 2 (2015), 146–150.
- [19] Angsheng Li and Yicheng Pan. 2016. Structural information and dynamical complexity of networks. *IEEE TIT* 62, 6 (2016), 3290–3339.
- [20] Zhikang Liu, Yiming Zhou, Yuansheng Xu, and Zilei Wang. 2023. Simplenet: A simple network for image anomaly detection and localization. In *CVPR*. 20402–20411.
- [21] Wenxin Ma, Xu Zhang, Qingsong Yao, Fenghe Tang, Chenxu Wu, Yingtai Li, Rui Yan, Zihang Jiang, and S Kevin Zhou. 2025. Aa-clip: Enhancing zero-shot anomaly detection via anomaly-aware clip. In *CVPR*. 4744–4754.
- [22] Pankaj Mishra, Riccardo Verk, Daniele Fornasier, Claudio Piciarelli, and Gian Luca Foresti. 2021. VT-ADL: A vision transformer network for image anomaly detection and localization. *arXiv preprint arXiv:2104.10036* (2021).
- [23] Alec Radford, Jong Wook Kim, Chris Hallacy, Aditya Ramesh, Gabriel Goh, Sandhini Agarwal, Girish Sastry, Amanda Askell, Pamela Mishkin, Jack Clark, et al. 2021. Learning transferable visual models from natural language supervision. In *ICML*. PmLR, 8748–8763.
- [24] Karsten Roth, Latha Pemula, Joaquin Zepeda, Bernhard Schölkopf, Thomas Brox, and Peter Gehler. 2022. Towards total recall in industrial anomaly detection. In *CVPR*. 14318–14328.
- [25] Mohammadreza Salehi, Niousha Sadjadi, Soroosh Baselizadeh, Mohammad H Rohban, and Hamid R Rabiee. 2021. Multiresolution knowledge distillation for anomaly detection. In *CVPR*. 14902–14912.
- [26] Claude Elwood Shannon. 1948. A mathematical theory of communication. *The Bell system technical journal* 27, 3 (1948), 379–423.
- [27] Dingli Su, Hao Peng, Yicheng Pan, and Angsheng Li. 2025. A survey of structural entropy: theory, methods, and applications. In *IJCAI*. 10660–10668.
- [28] Ashish Vaswani, Noam Shazeer, Niki Parmar, Jakob Uszkoreit, Llion Jones, Aidan N Gomez, Łukasz Kaiser, and Illia Polosukhin. 2017. Attention is all you need. *NeurIPS* 30 (2017).
- [29] Junran Wu, Xueyuan Chen, Bowen Shi, Shangzhe Li, and Ke Xu. 2023. Sega: Structural entropy guided anchor view for graph contrastive learning. In *ICML*. PMLR, 37293–37312.
- [30] Junran Wu, Xueyuan Chen, Ke Xu, and Shangzhe Li. 2022. Structural entropy guided graph hierarchical pooling. In *ICML*. PMLR, 24017–24030.
- [31] Chaoran Xu, Chengkan Lv, Qiyu Chen, Feng Zhang, and Zhengtao Zhang. 2026. MRAD: Zero-Shot Anomaly Detection with Memory-Driven Retrieval. *arXiv preprint arXiv:2602.00522* (2026).
- [32] Lewei Yao, Jianhua Han, Xiaodan Liang, Dan Xu, Wei Zhang, Zhenguo Li, and Hang Xu. 2023. Detclipv2: Scalable open-vocabulary object detection pre-training via word-region alignment. In *CVPR*. 23497–23506.
- [33] Ximiao Zhang, Min Xu, and Xiuzhuang Zhou. 2024. Realnet: A feature selection network with realistic synthetic anomaly for anomaly detection. In *CVPR*. 16699–16708.
- [34] Yiwu Zhong, Jianwei Yang, Pengchuan Zhang, Chunyuan Li, Noel Codella, Lianian Harold Li, Luowei Zhou, Xiyang Dai, Lu Yuan, Yin Li, et al. 2022. Regionclip: Region-based language-image pretraining. In *CVPR*. 16793–16803.
- [35] Qihang Zhou, Guansong Pang, Yu Tian, Shibo He, and Jiming Chen. 2024. AnomalyCLIP: Object-agnostic Prompt Learning for Zero-shot Anomaly Detection. In *ICLR*.
- [36] Jiawen Zhu, Yew-Soon Ong, Chunhua Shen, and Guansong Pang. 2025. Fine-grained abnormality prompt learning for zero-shot anomaly detection. In *ICCV*. 22241–22251.
- [37] Dongcheng Zou, Hao Peng, Xiang Huang, Renyu Yang, Jianxin Li, Jia Wu, Chunyang Liu, and Philip S Yu. 2023. Se-gsl: A general and effective graph structure learning framework through structural entropy optimization. In *WWW*. 499–510.
- [38] Yang Zou, Jongheon Jeong, Latha Pemula, Dongqing Zhang, and Onkar Dabeer. 2022. Spot-the-difference self-supervised pre-training for anomaly detection and segmentation. In *ECCV*. Springer, 392–408.

Appendix

A Datasets

We benchmark our method on 10 publicly available datasets that span two major application domains: industrial defect inspection and medical image analysis. All experiments strictly follow the ZSAD protocol, meaning the model is evaluated directly on the target test sets without accessing any in-distribution training data. Table 4 provides an overview of each dataset, covering its imaging modality, number of categories, and the distribution of normal and anomalous test samples. These benchmarks collectively encompass a wide variety of visual appearances, sensor types, and anomaly patterns, providing a rigorous evaluation of zero-shot generalization ability.

B Sensitivity Analysis

We further analyze the robustness of EntroAD with respect to several key hyperparameters, including fusion weights, loss weights, and router temperature. The results are illustrated in Fig. 4–6.

Analysis on Fusion Weights (α, β). We vary the fusion weight α for Branch A while setting $\beta = 1 - \alpha$. As shown in Fig. 4, the optimal fusion strategy differs across domains. Industrial datasets (e.g., MVTec-AD) favor a higher $\alpha \approx 0.7$, indicating that Branch A is more effective for structured anomaly patterns. In contrast, medical datasets (e.g., Kvasir) achieve better performance with a lower $\alpha \approx 0.3$, suggesting that Branch B plays a more important role in modeling complex and irregular anomalies. This divergence further supports the necessity of the dual-branch design for cross-domain adaptability.

Loss Weights (λ_A, λ_B). Figure 5 presents the effect of balancing branch-specific losses during Stage 2 training. We observe that $(\lambda_A, \lambda_B) = (0.7, 0.3)$ yields the most stable overall performance. Over-emphasizing the auxiliary branch slightly weakens the core visual-text alignment, particularly on industrial benchmarks, whereas the chosen configuration achieves a better trade-off between stability and adaptability.

Analysis on Router Temperature (T). As illustrated in Fig. 6, a moderate temperature around $T = 0.1$ provides the best balance between sharp and uniform token assignment. Lower temperatures lead to overly confident routing decisions, which may reduce diversity, while higher temperatures produce overly uniform distributions that dilute informative signals. Importantly, the performance remains relatively stable within the range $[0.05, 0.2]$, indicating that the routing mechanism is robust to moderate temperature variations.

Overall, the model demonstrates stable performance across a reasonably wide range of hyper-parameter settings, suggesting that EntroAD does not require delicate tuning and generalizes well under different configurations.

C Detailed Results

Tables 5–9 report per-category results on the five multi-class industrial benchmarks. For each dataset we provide image-level AUROC (I-AUROC) and Average Precision (I-AP), as well as pixel-level AUROC (P-AUROC) and Per-Region Overlap (P-AUPRO).

D Detailed Implementation Details

In the main text, we provided the core architecture and training paradigm. Here, we specify the remaining configuration details to ensure full reproducibility.

Architecture and Training Settings. Images and masks are resized to 518×518 . For multi-level feature extraction, we use the 6th, 12th, 18th, and 24th layers of the CLIP visual encoder. Stage 1 is trained for 1 epoch, followed by 5 epochs for Stage 2. We use the Adam optimizer with a learning rate of 4×10^{-4} and a batch size of 8. The branch loss weights are set to $\lambda_A = 0.7$ and $\lambda_B = 0.3$, and the router temperature is set to $T = 0.1$. For the frozen CLIP backbone, we maintain a default logit temperature of 0.07.

Inference and Post-processing. Based on the task-level prior, the fusion weights are explicitly assigned: Branch A dominates ($\alpha = 0.7, \beta = 0.3$) for structured anomalies, while Branch B is prioritized ($\alpha = 0.3, \beta = 0.7$) for diffuse patterns. To effectively suppress noisy background responses during the entropy-guided routing stage, we apply a confidence-aware gating threshold of $\tau = 0.5$, with steepness parameters empirically set to $k_0 = 5.0$ and $k_1 = 50.0$. Finally, the branch-specific anomaly maps are smoothed via a Gaussian filter ($\sigma = 4$), and the image-level anomaly scores are calculated by combining the top-1% pixel response and the cache-based score with a balancing factor of $k = 0.7$.

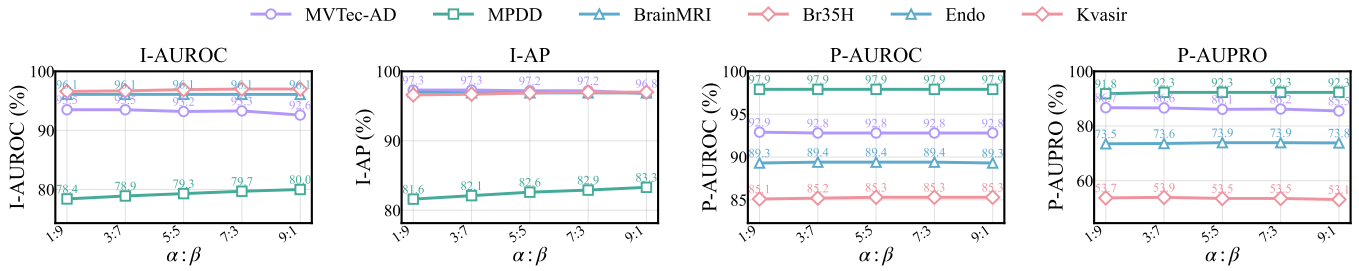


Figure 4: Effect of fusion weights (α, β) on anomaly detection performance across different scenarios.

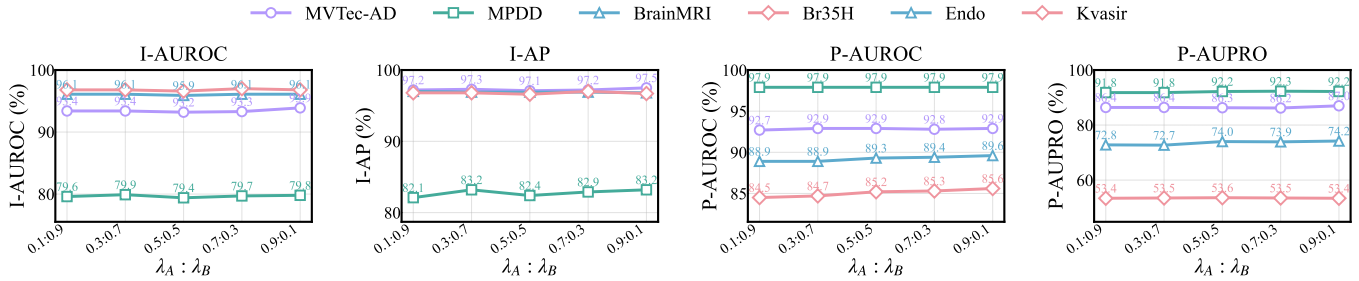


Figure 5: Effect of loss weights (λ_A, λ_B) on anomaly detection performance across different scenarios.

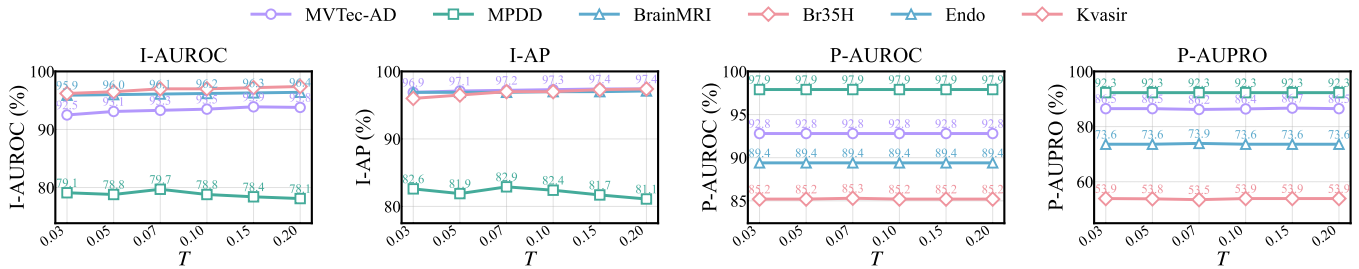


Figure 6: Effect of router temperature T on anomaly detection performance across different scenarios.

Table 4: Overview of the 10 datasets used for evaluation. We adopt the ZSAD protocol and only use test splits. Sample counts for MVtec AD and VisA correspond to their official test sets.

Domain	Dataset	Type	Modality	Cat.	Test Samples (Normal / Anomaly)
Industrial	MVTec AD [2]	Object & Texture	Photography	15	467 / 1258
	VisA [38]	Object	Photography	12	962 / 1200
	MPDD [16]	Object	Photography	6	176 / 282
	BTAD [22]	Object	Photography	3	451 / 290
	DTD [1]	Texture	Photography	12	357 / 947
Medical	HeadCT [25]	Brain	Radiology (CT)	1	100 / 100
	BrainMRI [18]	Brain	Radiology (MRI)	1	98 / 155
	Br35H [12]	Brain	Radiology (MRI)	1	1500 / 1500
	Kvasir [17]	Colon	Endoscopy	1	0 / 1000
	Endo [13]	Colon	Endoscopy	1	0 / 200

Table 5: Per-category results on MVTec AD (%).

Category	Image-level		Pixel-level	
	I-AUROC	I-AP	P-AUROC	P-AUPRO
<i>Textures</i>				
Carpet	100.0	100.0	99.3	98.2
Grid	99.2	99.7	98.4	92.9
Leather	100.0	100.0	99.3	98.4
Tile	99.6	99.8	97.2	93.0
Wood	99.0	99.7	97.7	93.6
<i>Objects</i>				
Bottle	94.3	98.3	91.1	83.8
Cable	95.2	97.3	79.3	67.6
Capsule	94.5	98.9	96.6	93.9
Hazelnut	96.6	98.3	96.3	93.1
Metal Nut	64.4	90.9	83.4	64.5
Pill	87.7	97.4	91.1	92.7
Screw	83.4	93.4	97.4	89.0
Toothbrush	98.1	99.3	95.3	88.8
Transistor	87.5	85.1	73.5	56.0
Zipper	99.7	99.9	96.7	88.2
Average	93.3	97.2	92.8	86.2

Table 6: Per-category results on VisA (%).

Category	Image-level		Pixel-level	
	I-AUROC	I-AP	P-AUROC	P-AUPRO
Candle	83.7	87.4	98.9	96.0
Capsules	92.7	96.0	95.5	78.4
Cashew	92.5	96.9	94.1	94.5
Chewinggum	98.6	99.4	99.6	94.9
Fryum	93.2	97.0	92.9	91.1
Macaroni1	81.1	82.7	98.6	92.6
Macaroni2	73.4	72.7	97.1	81.9
PCB1	76.6	79.7	90.6	82.8
PCB2	67.3	70.3	90.8	74.9
PCB3	68.2	71.9	88.3	79.1
PCB4	96.8	96.7	95.7	87.4
Pipe Fryum	91.9	96.1	96.1	94.9
Average	84.7	87.2	94.8	87.4

Table 7: Per-category results on MPDD (%).

Category	Image-level		Pixel-level	
	I-AUROC	I-AP	P-AUROC	P-AUPRO
Bracket Black	68.7	79.8	98.5	95.5
Bracket Brown	61.6	78.2	96.3	81.7
Bracket White	76.0	71.9	99.5	98.1
Connector	78.3	70.3	97.6	90.9
Metal Plate	96.4	98.6	97.5	94.0
Tubes	97.1	98.8	98.4	93.8
Average	79.7	82.9	97.9	92.3

Table 8: Per-category results on BTAD (%).

Category	Image-level		Pixel-level	
	I-AUROC	I-AP	P-AUROC	P-AUPRO
01	95.5	98.3	96.0	70.6
02	85.6	97.7	95.4	62.6
03	97.0	85.8	96.8	91.9
Average	92.7	93.9	96.1	75.1

Table 9: Per-category results on DTD (%).

Category	Image-level		Pixel-level	
	I-AUROC	I-AP	P-AUROC	P-AUPRO
Woven 001	100.0	100.0	99.8	96.5
Woven 127	95.4	96.7	96.2	92.6
Woven 104	98.9	99.7	97.0	92.5
Stratified 154	98.4	99.6	99.7	94.8
Blotchy 099	98.6	99.7	99.6	96.5
Woven 068	94.3	97.0	98.9	92.8
Woven 125	100.0	100.0	99.5	97.7
Marbled 078	99.1	99.8	99.3	97.6
Perforated 037	91.2	97.9	95.5	80.5
Mesh 114	85.9	94.5	97.2	84.8
Fibrous 183	98.7	99.7	99.5	98.5
Matted 069	89.6	97.2	99.3	85.9
Average	95.8	98.5	98.5	92.6